



Title	Performance characterization of the Inveon preclinical small-animal PET/SPECT/CT system for multimodality imaging
Author(s)	Magota, Keiichi; Kubo, Naoki; Kuge, Yuji; Nishijima, Ken-ichi; Zhao, Songji; Tamaki, Nagara
Citation	European Journal of Nuclear Medicine and Molecular Imaging, 38(4), 742-752 <a href="https://doi.org/10.1007/s00259-010-1683-y">https://doi.org/10.1007/s00259-010-1683-y</a>
Issue Date	2011-04
Doc URL	<a href="http://hdl.handle.net/2115/48719">http://hdl.handle.net/2115/48719</a>
Rights	The original publication is available at <a href="http://www.springerlink.com">www.springerlink.com</a>
Type	article (author version)
File Information	EJNMMI38-4_742-752.pdf



[Instructions for use](#)

Keiichi Magota<sup>1,2</sup>, Naoki Kubo<sup>3</sup>, Yuji Kuge<sup>4</sup>, Ken-ichi Nishijima<sup>4</sup>, Songji Zhao<sup>4</sup>, and  
Nagara Tamaki<sup>1</sup>

Performance characterization of the Inveon preclinical small-animal  
PET/SPECT/CT system for multi-modality imaging

<sup>1</sup>Department of Nuclear Medicine, Hokkaido University Graduate School of  
Medicine, Sapporo, Japan

<sup>2</sup>Department of Radiology, Hokkaido University Hospital, Sapporo, Japan

<sup>3</sup>Faculty of Health Sciences, Hokkaido University, Sapporo, Japan

<sup>4</sup>Department of Tracer Kinetics and Bioanalysis, Hokkaido University Graduate  
School of Medicine, Sapporo, Japan

Corresponding author: Keiichi Magota,

e-mail: [magota@huhp.hokudai.ac.jp](mailto:magota@huhp.hokudai.ac.jp), Tel: +81-11-7065150, Fax: +81-11-7067155,

Address: Kita 15 Nishi 7, Kita-ku, Sapporo 060-8638, Japan

Purpose: We analyzed the performance of the Inveon for an integrated small-animal PET/SPECT/CT system and compared the imaging capabilities of the SPECT and the PET components.

Methods: For SPECT, energy resolution, tomographic spatial resolution, and system sensitivity were evaluated with  $^{99m}\text{Tc}$  solution using a single pinhole collimator. For PET, spatial resolution, absolute sensitivity, scatter fraction, and peak noise equivalent count (NEC) were evaluated. A micro-Derenzo phantom, cylindrical phantom, and National Electrical Manufacturers Association NU-4 image quality phantom were scanned to compare SPECT and PET image capabilities, and SPECT and PET bone imaging were performed on a normal rat in vivo.

Results: SPECT spatial resolution was 0.84 mm full width at half maximum (FWHM) at a radius of rotation of 25 mm using the 0.5-mm pinhole aperture collimator, while PET spatial resolution was 1.63 mm FWHM at the center. SPECT system sensitivity at a radius of rotation of 25 mm was 35.3 cps/MBq ( $4 \times 10^{-3}\%$ ) using 0.5-mm pinhole aperture, while PET absolute sensitivity was 3.2% for 350–650 keV and 3.432 ns. Accordingly, the volume sensitivity of PET was three orders of magnitude

higher than that of SPECT.

Conclusions: This integrated PET/SPECT/CT system provided high system performance with excellent spatial resolution for SPECT and sensitivity for PET.

Based on tracer availability and system performance, SPECT and PET have complementary roles for multi-modality small-animal imaging.

Key Words: integrated PET/SPECT/CT system; small-animal imaging; performance measurement; instrumentation; molecular imaging

## INTRODUCTION

Molecular imaging of small laboratory animals using single photon emission tomography (SPECT), positron emission tomography (PET), and x-ray computed tomography (CT) has recently emerged as an important tool for the in vivo study of animal models of human disease. This imaging method enables longitudinal studies to be performed in the same animal, and animals can serve as their own control.

SPECT and PET have been used in functional imaging, including brain, heart, gene expression, and oncology studies [1, 2]. CT has also been used for anatomical imaging (e.g., bone imaging) because it provides high contrast between bone and soft tissue [3]. The use of SPECT, PET, and CT in combinations such as SPECT/CT, PET/CT, SPECT/PET, and SPECT/PET/CT—so-called “multi-modality imaging”—may enable the development of new and interesting protocols for investigating many biological phenomena more effectively than is possible using SPECT, PET, or CT modalities alone. Using these techniques, lesions visualized by functional imaging can be correlated with anatomic imaging. In general, CT is also used for attenuation and scatter correction of SPECT and PET images. However, in this

study, neither attenuation nor scatter correction was performed.

Integration of SPECT, PET, and CT images can be achieved by a “software approach” that fuses the images acquired by separate scanners. These techniques, however, are hampered by problems with object positioning and internal organ movement. Thus, animal movement and positioning of the holder require extreme care in the software approach. Alternatively, these problems can be addressed by using a “hardware approach”, which can be achieved by automatic imaging bed moving. The spatial transformation matrix for the registration is predetermined by a phantom scanning. A hardware approach would be the most useful and convenient method for small-animal imaging.

In the past several years, a large number of small-animal SPECT [4–8], PET [9–12], and CT systems have been developed and become commercially available. Moreover, efforts to develop trimodality preclinical systems integrated in a common gantry including SPECT/PET/CT also are under way. Examples of such a system are the FLEX Triumph™ imaging platform from Gamma Medica-Ideas and YAP(S)-PET [13]. Multi-modality systems are accessible with the same animal bed and image fusion can be obtained.

We have had the opportunity to use a new integrated PET/SPECT/CT system developed for molecular imaging of small animals in vivo. Several recent studies have reported the performance of the PET [14–17]; however, evaluation of the SPECT component and comparison of performance between PET and SPECT have not yet been reported.

It is known that SPECT using a pinhole collimator has high spatial resolution, while PET has high sensitivity. This feature plays an important role when deciding whether to use SPECT or PET. When integrated multi-modality imaging systems are used, it is particularly important to understand the features and performance of each modality and to choose the appropriate modality for a particular experiment, to obtain the best results. Therefore, it is necessary to compare performance between SPECT and PET in standard use, in terms of reconstruction methods and their parameters.

In the first two sections of this study, we aimed to evaluate the performance measurements of the SPECT component and validate the basic characterization of the PET component. In the final sections, we compare the capabilities of SPECT

and PET in terms of spatial resolution and sensitivity, respectively.

## MATERIALS AND METHODS

### System Description

We tested the latest commercially available small-animal imaging system (Inveon; Siemens Medical Solutions, Knoxville, TN). Inveon offers SPECT, PET, and CT imaging in dedicated, docked or integrated configurations to fit the research needs. Each performance is the same for all configurations. We have installed the integrated type SPECT/PET/CT system. In this configuration, the SPECT, PET, and CT components are combined in a common gantry, with SPECT and CT placed at the front and PET at the rear. The SPECT component is mounted perpendicularly to the CT component. The carbon fiber imaging bed has axial movement sufficient to image individually or with all three modalities in combination.

The SPECT component has dual head detector geometry that be mounted on a rotating gantry. Each detector head contains a 68 × 68 pixelated scintillator array of

2.0 × 2.0 × 10 mm NaI(Tl) crystals with 0.2 mm gap, in combination with a position-sensitive photomultiplier tube (PS-PMT) readout. The maximum active imaging region is 150 × 150 mm. Various interchangeable tungsten collimators can be attached to the detector: single pinhole collimators have aperture of 0.5, 1.0, 2.0, and 3.0 mm. The acceptance angle of the aperture is 90°, with focal length of 90 or 95 mm. The transaxial and axial field of view (FOV) varies with the radius of rotation from 28 to 45 mm. In the axial bed travel (continuous bed motion) mode, the axial FOV can be set larger ( $\leq 250$  mm). All counts are recorded and maintained in list mode to enable the use of various energy windows in postprocessing and reconstruction. Images can be reconstructed by three-dimensional ordered subset expectation maximization (3D-OSEM) or 3D maximum a posteriori (3D-MAP) method.

The PET component consists of 64 lutetium oxyorthosilicate (LSO) detectors arranged in 4 contiguous rings of 16 blocks with a ring diameter of 16.1 cm, to give an effective transaxial FOV of 10 cm and an axial FOV of 12.7 cm. Each detector consists of a 20 × 20 array of 1.5 × 1.5 × 10 mm LSO crystal elements coupled to a PS-PMT via a light guide. The scanner acquires exclusively in 3D mode. The

reconstruction methods have been described in detail in previous reports [14–17].

### Physical Study

We characterized the performance of the Inveon with regard to the SPECT and PET components. For SPECT, energy resolution, tomographic spatial resolution, and system sensitivity were evaluated. For PET, spatial resolution, absolute sensitivity, scatter fraction, and noise equivalent count (NEC) were evaluated. To compare the imaging capabilities of SPECT and PET, spatial resolution and sensitivity were evaluated using common phantoms: the micro-Derenzo phantom, cylindrical phantom, and National Electrical Manufacturers Association (NEMA) NU-4 image quality phantom [18]. Finally, to investigate in the practical animal-study, rat bone imaging was performed. Optimal imaging parameters (e.g., activity, acquisition time, and reconstruction settings) were not evaluated; therefore, these parameters were determined from visual evaluation of the rat bone images and the findings of previous reports [1, 2, 4–12]. The Inveon Acquisition Workplace 1.2.2.2 (Siemens Medical Solutions, Knoxville, TN) was used for SPECT and PET reconstruction.

## 1. SPECT

With regard to tomographic spatial resolution, and phantom and rat bone imaging (next section), projection data were acquired in step-and-shoot mode with 60 or 120 views over 360° at 30, 60, or 90 s/view. The acquisition time per view was prolonged according to the radioactivity decay. A 20% window was centered at the 140 keV photopeak of  $^{99m}\text{Tc}$ . The radius of rotation was 25, 30, or 35 mm. The 3D-OSEM algorithm method was used in reconstruction (number of iteration, 2; subsets, 6). Image matrix voxel size was 0.5 × 0.5 × 0.5 mm (0.2 × 0.2 × 0.2 mm for tomographic spatial resolution measurements). Neither attenuation nor scatter correction was performed. All reconstructed images were normalized using a correction matrix derived from a uniform cylindrical phantom imaged prior to reconstruction. Since the aperture sizes less than 1.0 mm of single pinhole collimator have been used in recent small-animal research [1, 4, 6, 7], this size only was evaluated in this study.

### 1.A. Energy Resolution

Crystal energy spectra within energy window of 0–300 keV were obtained

using a  $^{99m}\text{Tc}$  point source. A total of at least 10,000 counts were collected.

Energy resolution was determined for all crystals in the system and calculated as full width at half maximum (FWHM) of a 140 keV energy peak divided by the energy value.

### 1.B. Tomographic Spatial Resolution

Tomographic resolution was measured for the 0.5- and 1.0-mm pinhole aperture with a line source made from glass capillary tubes (inner diameter, 0.28 mm) filled with  $^{99m}\text{Tc}$  solution. The line source was mounted on the imaging bed and placed in the center of the transaxial FOV and aligned axially. Line-source images were obtained as a function of the radius of rotation, which varied in 5 mm steps from 25 to 35 mm. Projection data were acquired with 60 views over  $360^\circ$  at 60 s/view, for total acquisition time of 32 min.

Count profiles of the reconstructed transaxial images across the voxel having the maximum voxel intensity were plotted in the horizontal and vertical directions. FWHM and full width at tenth maximum (FWTM) were then determined by linear interpolation between adjacent pixels at a half or tenth, respectively, of the

profile maximum value, which was determined by parabolic fit using peak points and their two nearest neighboring points. The averages of horizontal and vertical direction were calculated simultaneously over 10 transaxial slices. The results of resolution measurements were not corrected for source dimension.

### 1.C. System Sensitivity

System sensitivity was measured in planar mode for the 0.5- and 1.0-mm pinhole apertures with a  $^{99m}\text{Tc}$  point source as a function of source to collimator distance, which varied in 5 mm steps from 25 to 35 mm. The point source was created by drawing a small fluid column into the tip of a 0.85 mm (inner diameter) capillary tube that was then mounted on the imaging bed, in the center of the transaxial and axial FOVs. Activity of the point source was approximately 0.5 MBq. During the acquisition time of 10 min, a total of at least 10,000 counts were collected in each measurement. System sensitivity was defined as the recorded counts per second divided by the decay-corrected activity of the point source.

## 2. PET

All performance measurements were set to a coincidence window of 3.432 ns and an energy window of 350–650 keV. Delayed events were subtracted from prompt events to correct for random events. The image matrix was  $256 \times 256 \times 159$ , resulting in voxel size of  $0.385 \times 0.385 \times 0.796$  mm ( $512 \times 512 \times 159$  matrix,  $0.215 \times 0.215 \times 0.796$  mm for spatial resolution measurements).

## 2.A. Spatial Resolution

Spatial resolution was measured using a  $^{22}\text{Na}$  point source with a nominal size of 0.6 mm, embedded in a Lucite disk. The activity of the point source was approximately 2.8 MBq. The point source was attached to the imaging bed and centered in the axial FOV. Data were acquired for 30 s in list mode at the center of the FOV and 2 cm radial offset position. All measurements were repeated four times. The images were reconstructed using Fourier rebinning algorithm (FORE) and filtered backprojection (FBP) with ramp filter cutoff at the Nyquist frequency. The method for calculating FWHM and FWTM was similar to that in the SPECT spatial resolution test (previous section). Results of the spatial resolution measurements were not corrected for source dimension, positron

range, or non-collinearity of positron annihilation.

## 2.B. Absolute Sensitivity

Absolute sensitivity was measured using a 15.0 cm glass tube with inner diameter of 1.0 mm that was filled with 4.8 MBq of  $^{18}\text{F}$ -FDG over 13.0 cm of its length. The glass line source was sealed at both ends and inserted into the smallest of a set of five concentric aluminum sleeves with wall thickness of 1.0 mm, and was scanned to determine sensitivity free from the effects of photon attenuation and scatter. Measurements were performed with the line source aligned along the scanner axis at the center. Data were acquired for each decreasing number of sleeves, and for 10 min. The number of coincidences was measured for intrinsic radioactivity from  $^{176}\text{Lu}$  in the LSO crystals were subtracted to obtain true counting rates, which were corrected for  $^{18}\text{F}$  activity decay. Sensitivity was extrapolated to zero wall thickness from an exponential fit to slice sensitivity plotted as a function of the number of sleeves [19].

## 2.C. Scatter Fraction and NEC

Scatter fraction and NEC were measured using two different cylindrical polyethylene phantoms to simulate a typical mouse (diameter, 3 cm; length, 7 cm) and rat (diameter, 6 cm; length, 15 cm). A 3.2 mm hole was drilled parallel to the central axis of the cylinder at a radial distance of 10 mm (mouse-like phantom) and 17.5 mm (rat-like phantom). A line-source insert with the same length as each phantom was filled with  $^{11}\text{C}$  solution and threaded through these holes. The phantoms were mounted on the imaging bed and placed in the center of the transaxial and axial FOVs [12].

Background coincidence events due to intrinsic radioactivity from  $^{176}\text{Lu}$  in the LSO crystals was also measured for 1 h with the mouse- or rat-like phantoms centered in the FOV, with no activity in the line source [20]. PET list mode data were sorted into two-dimensional (2D) sinograms using single-slice rebinning (SSRB). Prompt and random sinograms were generated separately. For prompt sinograms of each slice, each projection was shifted so that the pixel containing the maximum value was aligned with the central pixel of the sinogram. After alignment, a sum projection was produced such that a pixel in the sum projection is the sum of the pixels in each angular projection having the

same radial offset as the pixel in the sum projection. For each summed projection, all pixels in each sinogram located farther than 8 mm from the edge of the phantom were set to zero. All pixel counts beyond a 7 mm radius (line-source band) from the center of the profile were assumed to be the sum of random, scatter, and intrinsic counts; these counts under the peak were estimated by linearly interpolating the number of events at the left and right borders of the line-source band. Counts above this line were regarded as true counts. Random and intrinsic counts were estimated from random and blank sinograms, respectively, using the same band size of 16 mm larger than the phantom [9, 18]. The scatter counting rate and NEC have been used a methodology based on previous report [12]. Finally, peak NEC was determined for each phantom size.

## Comparative Study

### 1. Spatial Resolution

A micro-Derenzo phantom was scanned to compare image resolution. This phantom has an inner diameter of 32 mm and contains fillable hot rods of different

sizes (0.75, 1.00, 1.35, 1.70, 2.00, and 2.40 mm) arranged into six segments (Data Spectrum Corp). The phantom was filled with 37 MBq (5.3 MBq/mL) of  $^{18}\text{F}$ -FDG for PET scanning, or 111 MBq (15.9 MBq/mL) of  $^{99\text{m}}\text{Tc}$  solution for SPECT scanning. Acquisition time for PET scanning was 30 min. Sinograms were reconstructed using FORE and FBP into a  $256 \times 256 \times 159$  matrix. Attenuation and scatter correction were performed using a CT-based method. CT images were acquired in step-and-shoot mode. Acquisition parameters were as follows: voltage 80 kVp, anode current 500  $\mu\text{A}$ , angular sampling  $1^\circ$  per projection for a full  $360^\circ$  scan, and effective pixel size 186.1  $\mu\text{m}$ . Images were reconstructed using a modified Feldkamp algorithm. In SPECT scanning, 60 projection views were acquired at 60 s/view over  $360^\circ$ , with collimators of 0.5 and 1.0 mm aperture, at a radius of rotation of 30 mm. Total acquisition time was 32 min. Neither attenuation nor scatter correction was performed.

To calculate the recovery coefficient and estimate the fraction of the signal lost in the image due to resolution effects, we performed SPECT and PET scans of the NEMA NU-4 image quality phantom [18]. This phantom has a main fillable uniform region (inner diameter, 3.0 cm; length, 3.0 cm) and a solid acrylic glass region (inner

diameter, 3.0 cm; length, 2.0 cm) with five fillable rods drilled through with diameters of 1, 2, 3, 4, and 5 mm. The phantom was filled with 35 MBq (1.6 MBq/mL) of  $^{18}\text{F}$ -FDG for PET scanning, or 31 MBq (1.4 MBq/mL) of  $^{99\text{m}}\text{Tc}$  solution for SPECT scanning. For PET, the scan and reconstruction parameters were similar to those used for scanning the micro-Derenzo phantom. For SPECT, 120 projection views were acquired at 30 s/view over  $360^\circ$ , with a collimator of 0.5 mm aperture, at a radius of rotation of 35 mm. Total acquisition time was 32 min. Circular ROIs were then drawn in the reconstructed transaxial images for both SPECT and PET, around the main uniform region and for each rod. The recovery coefficient was defined as the mean value in each rod divided by the mean value obtained in the main uniform region. Simultaneously, the average and standard deviation of 10 axial slices was calculated.

## 2. Sensitivity

A cylindrical phantom was scanned to calculate volume sensitivity [21] and evaluate uniformity. The glass cylindrical phantom (inner diameter, 2.5 cm; length, 9 cm) was filled with 50 MBq (1.1 MBq/mL) of  $^{18}\text{F}$ -FDG for PET scanning, or 117 MBq

(2.6 MBq/mL) of  $^{99m}\text{Tc}$  solution for SPECT scanning. For PET, the scan and reconstruction parameters were similar to those used for scanning the micro-Derenzo phantom. For SPECT, 60 projection views were acquired at 90 s/view over 360°, with collimators of 0.5 and 1.0 mm aperture, at a radius of rotation of 25 mm. Total acquisition time was 48 min. Neither attenuation nor scatter correction was performed. Circular ROIs were then drawn in the reconstructed transaxial images of both the SPECT and PET images. Using the data from these ROIs, volume sensitivity was calculated as follows:

$$\text{Volume Sensitivity (cps/MBq/mL/cm)} = C_{\text{total}}/t/A/L, \quad \text{Eq. 1}$$

where  $C_{\text{total}}$  is the total counts in all projections with SPECT and the total true events in all systems with PET,  $t$  is mid-scan time,  $A$  is decay-corrected activity, and  $L$  is the axial length of a cylindrical phantom within an axial FOV. This method has been used previously for evaluating SPECT sensitivity in a clinical system [21]. For comparison, the PET data were then applied to this equation.

We calculated quantitative uniformity and the coefficient of

variation (CV) using the same ROI data. Quantitative uniformity was

calculated as follows:

$$\text{Uniformity (\%)} \square \frac{(\text{Max SPECT count} - \text{Min SPECT count})}{(\text{Max SPECT count} + \text{Min SPECT count})} \times 100, \text{ Eq. 2}$$

### 3. Animal Study

On the same day and in the same position, the same animal was scanned with CT,  $^{99m}\text{Tc}$ -methylene diphosphonate ( $^{99m}\text{Tc}$ -MDP) SPECT, and  $^{18}\text{F}$  PET. First, a normal rat (Sprague–Dawley, 165 g) was scanned with CT. Second, bone SPECT scanning was performed 2 h later, for 48 min, after injection of 96.9 MBq of  $^{99m}\text{Tc}$ -MDP. Finally, bone PET was performed 1 h later, for 30 min, after injection of 59.8 MBq of  $^{18}\text{F}$ . The rat was anesthetized with 1.0–1.5% isoflurane prior to imaging. The scan and reconstruction parameters used in CT and  $^{18}\text{F}$  PET scanning were similar to those used in scanning of the micro-Derenzo phantom. In  $^{99m}\text{Tc}$ -MDP SPECT scanning, 60 projection views were acquired at 90 s/view over 360°, with a collimator of 1.0 mm aperture, at a radius of rotation of 35 mm. Total acquisition time was 48 min. This animal study was performed in accordance with the guidelines for the care and use of laboratory animals of the Hokkaido University

Graduate School of Medicine.

## RESULTS

### Physical Study

#### 1. SPECT

Energy resolution for averaged over all crystals was 12.4%.

Fig. 1 shows the averages of horizontal and vertical tomographic spatial resolution as functions of the radius of rotation for the 0.5- and 1.0-mm pinhole aperture. Resolution for the 0.5-mm pinhole aperture was 0.84, 1.03, and 1.08 mm FWHM at a radius of rotation of 25, 30, and 35 mm, respectively, while resolution for the 1.0-mm pinhole aperture at each radius of rotation was 1.20, 1.25, and 1.27 mm, respectively.

System sensitivity as a function of source-to-collimator distance for the 0.5- and 1.0-mm pinhole aperture is plotted in Fig. 2. System sensitivity at a

source-to-collimator distance of 25 mm was 35.3 cps/MBq ( $4 \times 10^{-3}\%$ ) for the 0.5-mm pinhole aperture and 76.7 cps/MBq ( $9 \times 10^{-3}\%$ ) for the 1.0-mm pinhole aperture.

## 2. PET

The results of PET performance measurements are summarized in Table 1.

Horizontal and vertical spatial resolution were 1.63 and 1.64 mm FWHM, respectively, at the center of the FOV, and 2.16 and 2.26 mm FWHM, respectively, at radial offset of 2 cm.

At the center of the FOV, absolute sensitivity for energy windows of 350–650 keV using a coincidence window of 3.432 ns was 3.2%.

For an energy window of 350–650 keV and a coincidence window of 3.432 ns, scatter fraction and peak NEC were 13.6% and 1,394 kcps at 146 MBq for the mouse-like phantom, and 19.2% and 560 kcps at 97 MBq for the rat-like phantom, respectively.

Comparative Study

In comparing spatial resolution between PET and SPECT using reconstructed images of the micro-Derenzo phantom, the 1.70 mm hot rods could be distinguished visually on the PET image (Fig. 3b), while the 1.35 mm hot rods could be distinguished on SPECT with the 0.5-mm (Fig. 3c) and 1.0-mm pinhole aperture (Fig. 3d).

The recovery coefficients for SPECT using the 0.5-mm pinhole aperture and PET of each hot rod are shown in Fig. 4. The recovery coefficient for SPECT of the 0.5-mm pinhole aperture was greater than that for PET in all hot rods. Therefore, the results of the recovery coefficient study indicate that the partial volume effect was slightly less for SPECT than for PET.

Fig. 5 demonstrates image uniformity in the reconstructed images of the cylindrical phantom. No image contains any visible artifact. No residual systematic deviation is apparent from the center to the edge of the image.

Volume sensitivity as measured for SPECT with the 0.5- and 1.0-mm pinhole aperture and for PET was 2.0, 4.9, and  $3.7 \times 10^3$  cps/MBq/mL/cm, respectively, (Table 2), which indicates that volume sensitivity was three orders of magnitude

higher for PET than for SPECT.

Quantitative uniformity and CV measured for SPECT with the 0.5- and 1.0-mm pinhole aperture and for PET are summarized in Table 3. Quantitative uniformity measured for SPECT with the 0.5- and 1.0-mm pinhole aperture and for PET was 71.1, 37.0, and 23.8%, respectively. CV values were lower for PET (6.0%) than for SPECT (0.5-mm aperture, 18.0%; 1.0-mm aperture, 11.5%), which indicates greater uniformity for PET. Among the SPECT images, uniformity for the 1.0-mm pinhole aperture was better than for the 0.5-mm pinhole aperture.

Fig. 6 shows sagittal images of rat bone obtained by CT,  $^{18}\text{F}$  PET, and  $^{99\text{m}}\text{Tc}$ -MDP SPECT. Statistical noise was markedly lower in the  $^{18}\text{F}$  PET image (Fig. 6b) compared with the  $^{99\text{m}}\text{Tc}$ -MDP SPECT image (Fig. 6c). Bony structures, including the spine, vertebral canal, and sternum, were more clearly visible in the  $^{99\text{m}}\text{Tc}$ -MDP SPECT image than in the PET image.

## DISCUSSION

We studied the system performance and imaging capability of a new integrated PET/SPECT/CT system for molecular imaging of small animals in vivo. The performances of the PET component of this system has recently been reported [14–17]; however, this is the first report to evaluate SPECT performance in comparison with PET performance. We evaluated the full performance measurements of the SPECT component and validated the basic characterization of the PET component. By comparing SPECT and PET, we demonstrated the feasibility of the system for multi-modality imaging, and provided a basis for deciding whether to select SPECT or PET. A study using SPECT and PET has a number of potentials for molecular imaging with various types of suitable radiopharmaceuticals, but also for integrated molecular imaging using multiple radiopharmaceuticals at the same time. Of particular, molecular imaging in a pathology/physiology study, development of treatment strategy, therapeutic agents and methods and diagnostic probes/radiopharmaceuticals [22, 23] have been fully investigated in combination with perfusion imaging, including metabolic imaging, neuronal transporter-receptor imaging, angiogenesis, etc.  $^{99m}\text{Tc}$ -annexin A5, a new SPECT tracer as a marker of ongoing apoptotic cell death, and  $^{18}\text{F}$ -FDG, a standard

PET tracer as a marker of inflammation, are supposed to be useful in the detection of metabolically active atheroma. Zhao Y et al. [23] reported a comparison of the intralésional distribution of these tracers. In this development of a new diagnostic probe, comparative evaluation with standard probe is essential to understand its potentials and to show its superiority to standard probe. Therefore, when we interpret the results of SPECT and PET images, it is particularly important to understand the feature and performance of each modality.

The results of spatial resolution measurements and micro-Derenzo phantom imaging indicate that SPECT provides much better spatial resolution of reconstructed images than does PET (at a submillimeter scale). This is because PET has inherent limiting factors that degrade the resolution of reconstructed images, including those associated with the crystals (width, scattering, and penetration), photon non-collinearity, and positron range [24]. However, direct comparisons of spatial resolution between SPECT and PET are not appropriate because the size of the sources was different (0.25 mm in SPECT and 0.6 mm in PET). After correcting for source dimension, SPECT spatial resolution was 0.80, 1.00, 1.06 mm at a radius of rotation of 25, 30, and 35 mm, respectively, whereas

PET spatial resolution was 1.52 mm. Differences of spatial resolution were diminished but SPECT remained better than PET. In contrast, the advantage of PET over SPECT is that it exhibits a much higher sensitivity (by approximately three orders of magnitude) with respect to volume sensitivity. This advantage can be proven by the greater uniformity of PET for a lower CV value, using the cylindrical phantom, which occurs because SPECT requires physical collimators to reject photons [24]. The image quality of the rat bone study showed good agreement with these findings. Thus, the performances of SPECT and PET are complementary. The trade-off relation between resolution and sensitivity was in agreement with a previous report [24]. These features offer biomedical scientists important information for selecting SPECT or PET, with regard to physical characteristics and pharmaceutical selections.

To compare the sensitivities of SPECT and PET, we measured volume sensitivity from the cylindrical phantom. The emitted photons suffer attenuation and scattering by the water in the cylindrical phantom. This effect is dependent on the emitted radiation energy, object size, and material. Although volume sensitivity includes the effects of attenuation and scatter, we consider that this method is suitable for

evaluating final image feasibility in comparing SPECT and PET. Because this measurement method is easy and convenient, we suggest that this method should be used to compare sensitivity between SPECT and PET.

With regard to SPECT performance measurements, tomographic spatial resolution was in general agreement with the results obtained from other small-animal scanners [4, 5], for the same aperture size and radius of rotation. Our results for system sensitivity were also in general agreement with those for other small-animal scanners equipped with a single pinhole collimator and the same aperture size and radius of rotation [4, 7]. Comparison to the latest small-animal SPECT system with their much number of detectors and pin-holes such as U-SPECT-II [6], and NanoSPECT [25], these systems provide much higher sensitivity than the Inveon SPECT. The energy resolution was worse for this system as compared with the semiconductor system (12.4%–5.6%) [11], which was comparable to the same Anger-type system [7, 12]. The present results for tomographic spatial resolution and system sensitivity less lower than that for manufacturers datasheets. Because energy window, reconstruction setting, etc. may be different to those used in our measurement.

With regard to PET performance measurements, the present results for spatial resolution differ slightly from those reported in previous studies [14–16] in which the results were obtained from  $^{22}\text{Na}$  point-source images. Because the diameters of these sources are different to those used in our measurements, direct comparison is not appropriate. We measured absolute sensitivity, free of photon attenuation and scatter, using an extrapolation method [19]. Absolute sensitivity in our study was comparable to the previous study [17]. The present results for scatter fraction and peak NEC differ slightly from those reported in previous studies because we used cylindrical phantoms of differing diameters. We used phantoms with slightly larger diameters than those reported in previous studies [15–17].

Improvement in PET resolution is generally limited by positron range, particularly in small-animal scanners. The MAP reconstruction method has the advantage of being able to include the entire positron range directly into the algorithm. SPECT using a pinhole collimator is an exciting example of a technological advance that introduces the possibility of enhanced image resolution. It must be noted, however, that using a pinhole collimator with a small aperture results in decreased sensitivity. A multi-pinhole collimator has the potential to improve sensitivity. The Inveon

permits the use MAP reconstruction in PET and a multi-pinhole collimator in SPECT; thus, these are topics for further study.

In the present study,  $^{99m}\text{Tc}$ -MDP SPECT showed higher spatial resolution, while  $^{18}\text{F}$  PET showed higher sensitivity, consistent with our physical measurements. Other tracers, however, are used in SPECT imaging for animal research.  $^{125}\text{I}$  and  $^{111}\text{In}$ , for example, have attractive chemical properties and are commonly used in molecular biology for labeling of nucleic acids, antibodies, ligands, and other pharmaceuticals. Spatial resolution and sensitivity in SPECT using a pinhole collimator are changed by isotope energy because of aperture penetration [6]. In addition, the results of SPECT and PET performance, particularly spatial resolution and imaging studies, are influenced by the employed image reconstruction methods and parameters (iteration, subset, etc.) [14]. Thus, in future research it will be necessary to evaluate these performance tests, using the alternative tracers and the reconstruction methods and parameters.

## CONCLUSION

This study evaluated the performance of a new integrated PET/SPECT/CT system for small-animal imaging with regard to the SPECT and PET components.

This system provided high system performance with excellent spatial resolution for SPECT and sensitivity for PET. Based on tracer availability and system performance, SPECT and PET have complementary roles in multi-modality small-animal imaging.

#### ACKNOWLEDGMENTS

The authors would like to thank Kotaro Suzuki and Kyotaro Suzuma for assisting with data collection.

#### CONFLICT OF INTEREST STATEMENT

I declare no conflict of interest.

## REFERENCES

1. Liu Z, Kastis GA, Stevenson GD, Barrett HH, Furenlid LR, Kupinski MA, et al. Quantitative analysis of acute myocardial infarct in rat hearts with ischemia-reperfusion using a high-resolution stationary SPECT system. *J Nucl Med* 2002;43:933–9.
2. Inubushi M, Wu JC, Gambhir SS, Sundaresan G, Satyamurthy N, Namavari M, et al. Positron-emission tomography reporter gene expression imaging in rat myocardium. *Circulation* 2003;107:326–32.
3. Waarsing JH, Day JS, van der Linden JC, Ederveen AG, Spanjers C, De Clerck N, et al. Detecting and tracking local changes in the tibiae of individual rats: a novel method to analyse longitudinal in vivo micro-CT data. *Bone* 2004;34:163–9.
4. McElroy DP, MacDonald LR, Beekman FJ, Wang YC, Patt BE, Iwanczyk JS, et al. Performance evaluation of A-SPECT: a high resolution desktop pinhole SPECT system for imaging small animals. *IEEE Trans Nucl Sci* 2002;49:2139–47.
5. Weber DA, Ivanovic M, Franceschi D, Strand SE, Erlandsson K, Franceschi M,

- et al. Pinhole SPECT: an approach to in vivo high resolution SPECT imaging in small laboratory animals. *J Nucl Med* 1994;35:342–8.
6. van der Have F, Vastenhouw B, Ramakers RM, Branderhorst W, Krah JO, Ji C, et al. U-SPECT-II: an ultra-high-resolution device for molecular small-animal imaging. *J Nucl Med* 2009;50:599–605.
  7. Zeniya T, Watabe H, Aoi T, Kim KM, Teramoto N, Takeno T, et al. Use of a compact pixellated gamma camera for small animal pinhole SPECT imaging. *Ann Nucl Med* 2006;20:409–16.
  8. Kubo N, Zhao S, Fujiki Y, Kinda A, Motomura N, Katoh C, et al. Evaluating performance of a pixel array semiconductor SPECT system for small animal imaging. *Ann Nucl Med* 2005;19:633–9.
  9. Tai YC, Chatziioannou A, Siegel S, Young J, Newport D, Goble RN, et al. Performance evaluation of the microPET P4: a PET system dedicated to animal imaging. *Phys Med Biol* 2001;46:1845–62.
  10. Knoess C, Siegel S, Smith A, Newport D, Richerzhagen N, Winkeler A, et al. Performance evaluation of the microPET R4 PET scanner for rodents. *Eur J Nucl Med Mol Imaging* 2003;30:737–47. doi:10.1007/s00259-002-1052-6.

11. Kim JS, Lee JS, Im KC, Kim SJ, Kim SY, Lee DS, et al. Performance measurement of the microPET focus 120 scanner. *J Nucl Med* 2007;48:1527–35. doi:10.2967/jnumed.107.040550.
12. Tai YC, Ruangma A, Rowland D, Siegel S, Newport DF, Chow PL, et al. Performance evaluation of the microPET focus: a third-generation microPET scanner dedicated to animal imaging. *J Nucl Med* 2005;46:455–63.
13. Del Guerra A, Bartoli A, Belcari N, Herbert D, Motta A, Vaiano A, et al. Performance evaluation of the fully engineered YAP-(S)PET scanner for small animal imaging. *IEEE Trans Nucl Sci* 2006;53:1078–83. doi:10.1109/TNS.2008.2002257.
14. Visser EP, Disselhorst JA, Brom M, Laverman P, Gotthardt M, Oyen WJG, et al. Spatial resolution and sensitivity of the Inveon small-animal PET scanner. *J Nucl Med* 2009;50:139–47. doi:10.2967/jnumed.108.055152.
15. Bao Q, Newport D, Chen M, Stout DB, Chatziioannou AF. Performance evaluation of the Inveon dedicated PET preclinical tomograph based on the NEMA NU-4 standards. *J Nucl Med* 2009;50:401–8. doi:10.2967/jnumed.108.056374.

16. Kemp BJ, Hruska CB, McFarland AR, Lenox MW, Lowe VJ. NEMA NU2-2007 performance measurements of the Siemens Inveon™ preclinical small animal PET system. *Phys Med Biol* 2009;54:2359–76. doi:10.1088/0031-9155/54/8/007.
17. Constantinescu CC, Mukherjee J. Performance evaluation of an Inveon PET preclinical scanner. *Phys Med Biol* 2009;54:2885–99. doi:10.1088/0031-9155/54/9/020
18. National Electrical Manufacturers Association (NEMA). Performance Measurements of Small Animal Positron Emission Tomographs. NEMA Standards Publication NU4-2008. Rosslyn, VA: National Electrical Manufacturers Association; 2008.
19. Bailey DL, Jones T, Spinks TJ. A method for measuring the absolute sensitivity of positron emission tomographic scanners. *Eur J Nucl Med* 1991;18:374–9.
20. Watson CC, Casey ME, Eriksson L, Mulnix T, Adams D, Bendriem B. NEMA NU 2 performance tests for scanners with intrinsic radioactivity. *J Nucl Med* 2004;45:822–6.
21. Kouris K, Clarke GA, Jarritt PH, Townsend CE, Thomas SN. Physical

- performance evaluation of the Toshiba GCA-9300A triple-headed system. J Nucl Med 1993; 34:1778–89.
22. Kuge Y, Yokota C, Tagaya M, Hasegawa Y, Nishimura A, Kito G, et al. Serial changes in cerebral blood flow and flow-metabolism uncoupling in primates with acute thromboembolic stroke. J Cereb Blood Flow Metab 2001;21:202–10.
23. Zhao Y, Kuge Y, Zhao S, Morita K, Inubushi M, Strauss HW, et al. Comparison of <sup>99m</sup>Tc-annexin A5 with <sup>18</sup>F-FDG for the detection of atherosclerosis in ApoE–/– mice. Eur J Nucl Med Mol Imaging 2007;34:1747–55.  
doi:10.1007/s00259-007-0433-2.
24. Rahmim A, Zaidi H. PET versus SPECT: strengths, limitations and challenges. Nucl Med Commun 2008;29:193–207.
25. Del Guerra A, Belcari N. State-of-the-art of PET, SPECT and CT for small animal imaging. Nucl Instr Methods A 2007;583:119–24.  
doi:10.1016/j.nima.2007.08.187.

Table 1. Summary of the Results of PET Performance Measurements

<b>Spatial resolution</b>	<b>Absolute sensitivity</b>	<b>Scatter fraction <sup>c</sup></b>	<b>Peak NEC <sup>c</sup></b>
<b>(mm)</b>	<b>(%)</b>	<b>(%)</b>	<b>(kcps at MBq)</b>
Center of FOV	350–650 keV, 3.432 ns	Mouse-like phantom <sup>d</sup>	Mouse-like phantom <sup>d</sup>
1.63 <sup>a</sup> , 1.64 <sup>b</sup>	3.2	13.6	1,394 at 146
2 cm radial offset		Rat-like phantom <sup>e</sup>	Rat-like phantom <sup>e</sup>
2.16 <sup>a</sup> , 2.26 <sup>b</sup>		19.2	560 at 97

<sup>a</sup> Tangential direction

<sup>b</sup> Radial direction

<sup>c</sup> Scatter fraction and peak NEC were obtained at an energy window setting of 350–650 keV and coincidence window of 3.432 ns.

<sup>d</sup> Diameter = 30 mm, length = 70 mm

<sup>e</sup> Diameter = 60 mm, length = 150 mm

Table 2. Comparison of Volume Sensitivity between SPECT and PET

	<b>Pinhole aperture size</b>	<b>Volume sensitivity</b>
	<b>(mm)</b>	<b>(cps/MBq/mL/cm)</b>
SPECT	0.5	2.0
	1.0	4.9
PET	–	$3.7 \times 10^3$

Table 3. Comparison of Quantitative Uniformity and CV between SPECT and PET

	Pinhole aperture size	Quantitative uniformity	CV
	(mm)	(%)	(%)
SPECT	0.5	71.1	18.0
	1.0	37.0	11.5
PET	–	23.8	6.0

## Figure legends

Fig. 1 Tomographic spatial resolution in SPECT as a function of radius of rotation for 0.5- and 1.0-mm aperture size. FWHM = full width at half maximum. FWTM = full width at tenth maximum.

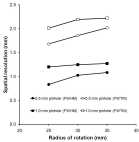
Fig. 2 System sensitivity in SPECT as a function of source-to-collimator distance for different pinhole aperture sizes. cps = counts per second.

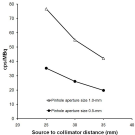
Fig. 3 Images of the micro-Derenzo phantom obtained by each modality. (a) CT: with contrast material, (b) PET, (c) SPECT: pinhole aperture size of 0.5 mm, and (d) SPECT: pinhole aperture size of 1.0 mm. (Rod diameter = 0.75, 1.0, 1.35, 1.7, 2.0, and 2.4 mm).

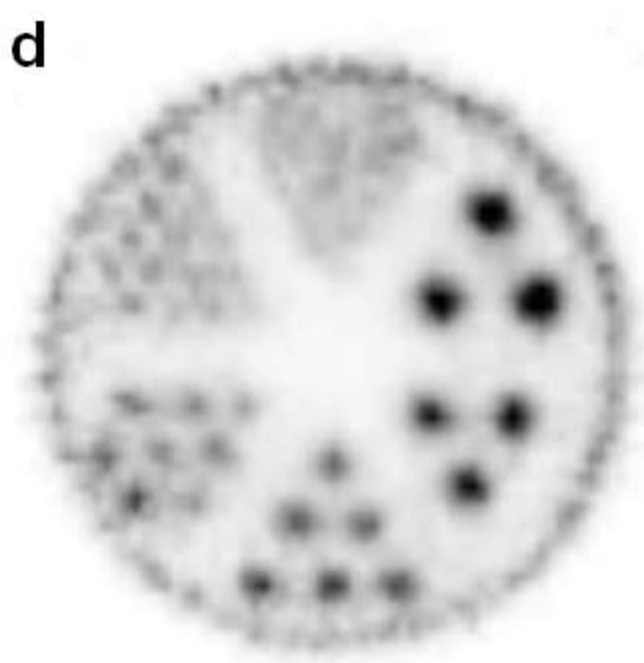
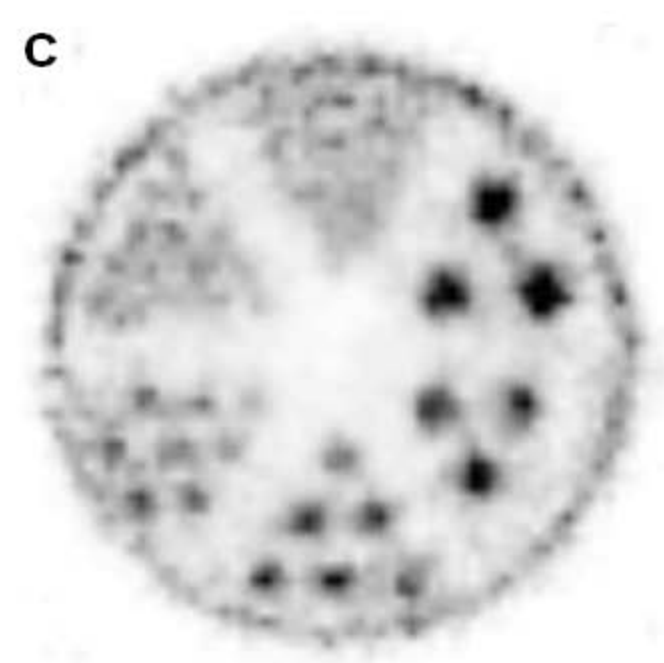
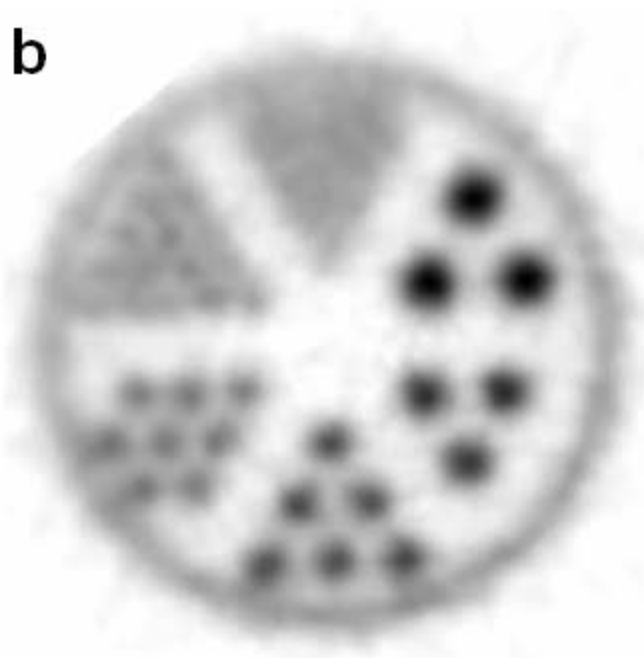
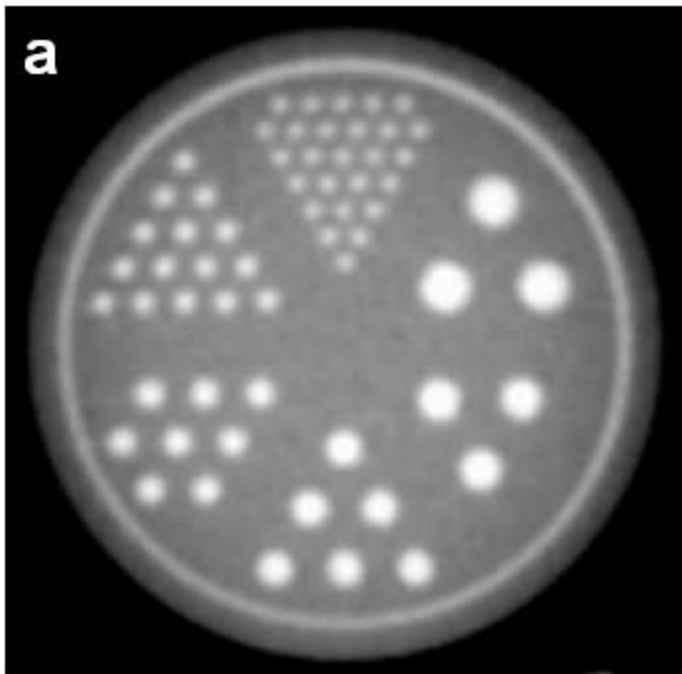
Fig. 4 Recovery coefficient as a function of rod diameter for PET and SPECT (pinhole aperture size of 0.5 mm).

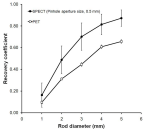
Fig. 5 Images of the cylindrical phantom obtained by each modality. (a) PET, (b) SPECT: pinhole aperture size of 0.5 mm, and (c) SPECT: pinhole aperture size of 1.0 mm.

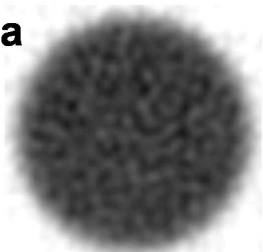
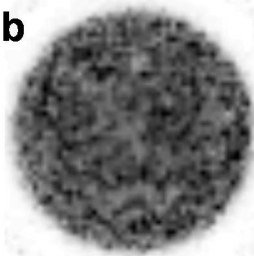
Fig. 6 Sagittal images of rat bone. (a) CT, (b)  $^{18}\text{F}$  PET, and (c)  $^{99\text{m}}\text{Tc}$ -MDP SPECT: pinhole aperture size of 1.0 mm.









**a****b****c**